

Measurements of the thermal, dielectric, piezoelectric, pyroelectric and elastic properties of  
porous PZT samples

Sidney B. Lang<sup>1\*</sup> and Erling Ringgaard<sup>2</sup>

<sup>1</sup>Dept. of Chemical Engineering, Ben-Gurion University of the Negev, 84105 Beer Sheva,  
Israel

<sup>2</sup>Meggitt Sensing Systems, Hejreskovvej 18A, DK-3490 Kvistgård, Denmark

The introduction of porosity into ferroelectric ceramics has been of great interest in recent years. In particular, studies of porous lead-zirconate-titanate ceramic (PZT) have been made. In the research reported, samples of Ferroperm Pz27 with porosities of 20, 25 and 30% were studied. Very complete measurements were made of all of the physical properties relevant for ferroelectric applications including thermal conductivity and diffusivity, heat capacity, dielectric, pyroelectric, piezoelectric and elastic properties. Scanning electron micrographs indicated a change from 3-0 to 3-3 connectivity with increasing porosity. Although most of the physical properties are degraded by the presence of porosity, both piezoelectric and pyroelectric figures-of-merit are improved because of the markedly reduced relative permittivity. Porous ferroelectric ceramics are very promising materials for a number of applications.

\*E-mail: [lang@bgu.ac.il](mailto:lang@bgu.ac.il), Fax: +972-8-6472916

## 1. Introduction

The effect of porosity on the physical properties of ferroelectric ceramics has been of significant interest in recent years. Because of its technological importance, porous lead-zirconate-titanate ceramic (PZT) has been studied extensively [1-15]. The porosity is created by the introduction of organic particles such as polymethyl methacrylate, methyl ethyl cellulose, camphene, starch, graphite and others. Porous piezoceramics are relevant for a number of applications due to interesting thermal, dielectric, pyroelectric, piezoelectric and elastic physical properties. In the case of ultrasonic transducers (e.g., transducers for medical diagnostics and air transducers), the main requirements for the piezoelectric material are as follows:[16]

- high electromechanical thickness coupling factor  $k_t$  and low transverse coupling factor
- permittivity in a suitable range, depending on the frequency and driving electronics
- mechanical quality factor  $Q_m$  as low as possible in order to obtain a large bandwidth
- acoustic impedance as low as possible for close acoustic matching to the propagation medium (e.g.,  $Z_a(\text{water}) = 1.5 \text{ MRayl}$ ,  $Z_a(\text{air}) = 0.4 \text{ kRayl}$ )

Another relevant example is hydrophones, where the most important parameters are acoustic impedance and hydrostatic figure-of-merit (to be discussed below). The presence of porosity in piezoceramics is known to reduce the transverse coupling factor without affecting the thickness coupling severely, and at the same it increases mechanical damping and thereby reduces  $Q_m$ . As would be expected, also the acoustic impedance and permittivity are significantly reduced by the introduction of pores in the ceramic matrix.

Similarly, for pyroelectric applications, the main requirements are:[10, 11, 13, 17]

- high pyroelectric coefficient
- low dielectric permittivity, especially at low frequencies
- low dielectric loss tangent, especially at low frequencies

We studied samples of Ferroperm® Pz27 with porosities of 20, 25 and 30%. Pz27 is a soft piezoelectric ceramic made by Meggitt Sensing Systems, Denmark [18]. Thermal, dielectric, piezoelectric, pyroelectric and elastic properties were measured. The samples were examined with a scanning electron microscope. Pyroelectric and piezoelectric figures-of-merit were calculated for the various materials.

## **2. Materials**

The PZT materials studied were Ferroperm® Pz27, a piezoelectric ceramic with a composition close to that of the morphotropic phase boundary (MPB) with a Zr/Ti ratio of about 52/48. They were prepared using conventional ceramic processing techniques but with the addition of organic particles which were burned out before sintering to yield samples with porosities of 20, 25 and 30%. Fired-on silver electrodes were applied and the samples were poled while immersed in a non-conducting poling fluid. In addition, a commercial sample of Pz27 was studied. It had a porosity of about 4% and is referred to in this paper as “dense” material. The properties were measured on samples that were 16 mm in diameter and 1 mm thick. Scanning electron micrographs of all of the materials are shown in Fig. 1. Newnham and co-workers introduced the concept of connectivity in 1978 for classifying two-phase composites [19]. They found that there were ten types of diphasic composites, each identified by a two-digit notation. The first digit represents the active phase and the second, the inactive phase. The connectivities of the porous materials shown in Fig. 1 appeared to be a mixture of 3-0 and 3-3 where the active phase was the PZT and the inactive phase was a mixture of poling fluid and air.

### 3. Property Measurements

#### 3.1. Thermal Diffusivity and Conductivity

The thermal diffusivities of the samples were measured by a technique [20] that is a modification of ones originally developed by Lang [21] and Muensit and Lang [22]. The test sample is affixed by a very thin layer of silver paint to a pyroelectric thermal detector. The top surface of the test sample is exposed to a laser beam whose intensity is modulated at various frequencies. The energy of the beam is absorbed in a black absorption layer and the heat diffuses into the sample in the form of a fluctuating temperature wave superimposed on a steady-state gradient. The temperature fluctuations or thermal waves are attenuated as they travel through the sample and they are also retarded in phase. The phase of the thermal waves as they exit from the test sample is determined relative to the phase of the laser beam by means of the pyroelectric detector. Because only the phase is determined, both the detector pyroelectric coefficient and the laser beam intensity cancel out in the analysis and are not required. The pyroelectric detector was either a disk of dense Pz27 or a disk of porous material with the same porosity as the test sample. The sample structures were placed in an HFS91 Heating and Freezing Stage (Linkam Scientific Instruments, Ltd., UK) whose temperature was varied from 213 to 423 K. A Lisa HL25/M1 diode laser (Lisa Laser Products, Germany) with a power of 25 mW and a wavelength of 685 nm was used to heat the samples. A Stanford Research SR850 Lock-in Amplifier (Stanford Research Systems, USA) produced a sine wave output voltage to drive the laser modulator and also measured the real and imaginary components of the pyroelectric current from which the phase lag was calculated. Thermal conductivity,  $k$ , is a more fundamental property than thermal diffusivity,  $\alpha$ . The two quantities are related by  $\alpha = k / (\rho c)$  where  $\rho$  is density and  $c$  is the heat capacity per unit mass (SI units are used throughout). Heat capacity data in the range from 1.8 to 400 K were measured using thermal relaxation calorimetry [23] and from 400 to 423 K using differential scanning calorimetry (DSC) [20]. Density data were obtained from [24]. The thermal conductivities for the three porous samples and the dense sample are shown in Fig. 2. The temperature dependence of the thermal conductivities is weak but the conductivities decrease markedly with increasing porosity.

#### 3.2. Pyroelectric coefficients

The pyroelectric coefficients were determined at specific temperatures by a combination of the Lang-Steckel [25] and the Byer-Roundy methods [26] using the following procedure. The samples were placed in the Heating and Freezing Stage and the stage temperature was cycled up and down over the range from 293 to 343 K six times at the rate of 1 K min<sup>-1</sup>. The pyroelectric current was measured with a picoammeter (Keithley Model 487, USA). The pyroelectric coefficients were calculated at the temperatures 300, 310, 320 and 330 K using the following equation

$$I = pA \frac{dT}{dt} \quad (1)$$

where  $I$  = pyroelectric current,  $p$  = pyroelectric coefficient,  $A$  = electrode area of the sample and  $dT/dt$  = rate of temperature change. Then the temperature range was extended from -60 to 150°C by use of the Chynoweth method [27]. In this procedure, the samples were held at each of the four temperatures and were exposed to radiation from a 30 mW diode laser beam that was modulated sinusoidally at a frequency of 10 Hz. The pyroelectric current was measured with the lock-in amplifier. The  $dT/dt$  was calculated from the previously determined pyroelectric coefficients using Eqn. (1) and the four values were averaged. Then the current produced by the laser heating was measured as the temperature was varied over the entire temperature range. Using the average  $dT/dt$ , the pyroelectric coefficient was determined from -60 to 150°C as shown in Fig. 3. The pyroelectric coefficients increase with increasing temperature and decrease strongly with increasing porosity.

### **3.3. Permittivity and Loss Tangent**

The  $\epsilon_{33}$  relative permittivity or dielectric constant and the dielectric loss  $\tan \delta$  were determined at room temperature on all of the samples using an impedance analyzer (Agilent 4194A). The frequency range was from 10 Hz to 10 kHz. The relative permittivity and the loss tangent are shown in Figs. 4 and 5, respectively. The permittivity varied only slightly over the frequency range with a small increase at very low frequencies. The permittivity values decreased markedly with increasing sample porosity. The loss tangents were between 0.01 and 0.02 for all frequencies. They increased slightly with frequency and decreased slightly with porosity.

### 3.4 Piezoelectric and Elastic Properties

Complex piezoelectric and elastic properties were determined according to the procedures of Alguero *et al.* [28] using thin disk-shaped samples. As described by Holland [29], the losses occurring in piezoelectric materials may be dielectric, elastic or piezoelectric and all of these may be represented by extending the various coefficients into complex ones. This is well known for the dielectric (cf.  $\tan \delta_e$  above) and elastic losses, and similarly the phenomenological piezoelectric loss should be understood as imperfect piezoelectric energy conversion. Thus a piezoelectric loss tangent may be defined as (with the  $d$  coefficient as example) the ratio between the imaginary (loss) component and the real one:  $\tan \delta_p = d''/d'$ . Resonances were measured using an impedance analyzer (Agilent 4194A). The thickness resonances of a disk that was poled and excited along its thickness were used to determine the  $c_{33}^D$  elastic stiffness coefficient, the  $k_t$  and  $k_{31}$  coupling coefficients. The radial resonances of the same disk were used to determine the  $c_{11}^D$  elastic stiffness coefficient, the  $d_{31}$  piezoelectric charge and  $g_{31}$  voltage coefficients and the  $k_p$  coupling coefficient. Since only thin disks were available, the  $d'_{33}$  piezoelectric charge coefficient was measured at 110 Hz using a  $d_{33}$  meter (Sinocera YE2730). The  $g'_{33}$  piezoelectric voltage coefficient was calculated from  $d_{33} = g_{33} \epsilon_{33}^T$ . The piezoelectric charge coefficients are shown in Fig. 6. The  $d_{31}$  coefficient decreases with increasing porosity whereas the  $d_{33}$  coefficient is relatively constant. Rybyanets [15] explained that the decrease in the  $d_{31}$  coefficient was caused by the disturbance of the quasi-rod skeleton continuity in the lateral direction. On the other hand, the near constancy of the  $d_{33}$  coefficient resulted because the relative decrease in the relative surface area of the ceramic phase was compensated by an increase in the relative pressure applied to the ceramic skeleton. The planar Poisson's ratio ( $\sigma$ ) varies only slightly with porosity (Fig. 7). The  $k_p$  and  $k_{31}$  coupling coefficients shown in Fig. 7 decrease with porosity but the  $k_t$  coefficient remains constant. The  $k_p$  and  $k_{31}$  coupling coefficients are related to the Poisson's ratio by the equation [30]:

$$k_p = a k_{31} \text{ where } a = \left( \frac{2}{1-\sigma} \right)^{1/2} \quad (2)$$

The experimental data were in excellent agreement with this equation. The Poisson's ratio has a negligibly small imaginary part and therefore can be considered as a real number. We now expand  $\tan \delta(k_p)$  and insert Eqn. (2) obtaining the third term in Eqn. (3). Because  $a$  is a real quantity, it can be taken outside of the real and imaginary operators (fourth term in Eqn. (3)) where it is cancelled out, finally yielding  $\tan \delta(k_{31})$ .

$$\tan \delta(k_p) = \frac{\text{Im}(k_p)}{\text{Re}(k_p)} = \frac{\text{Im}(a k_{31})}{\text{Re}(a k_{31})} = \frac{a \text{Im}(k_{31})}{a \text{Re}(k_{31})} = \tan \delta(k_{31}) \quad (3)$$

Thus the loss tangents of  $k_p$  and  $k_{31}$  are equal as shown in Fig. 7. Both the  $c_{33}^D$  and  $c_{33}^E$  elastic stiffness decrease with porosity, as illustrated in Fig. 8.

#### 4. Figures of merit

As shown in the graphs, almost all of the properties decrease with increasing porosity. At first glance, this would appear to be disadvantageous for applications. However, the equations that describe the functioning of various devices contain combinations of physical properties called figures-of-merit. These may be enhanced in porous materials despite the fact that the individual physical properties are reduced. Table I gives the equations for four figures-of-merit [31] for pyroelectric devices. The parameter  $\epsilon_0$  is the permittivity of free space ( $8.8542 \times 10^{-12} \text{ F m}^{-1}$ ). The dielectric constant and loss tangent at 1 kHz were used in the pyroelectric figure-of-merit calculations. The voltage and current figures-of-merit for the different porosities are shown in Fig. 9 and the detectivity and imaging figures-of-merit are illustrated in Fig. 10. The voltage figure-of-merit is important in pyroelectric infrared detectors in which a high-impedance amplifier is used. The current figure-of-merit is relevant for low-impedance amplifiers. The detectivity figure-of-merit is useful in applications with high-impedance amplifiers where the pyroelectric element is the principal noise source. The imaging figure-of-merit is relevant for pyroelectric imaging devices. The presence of porosity increases the voltage, imaging and detectivity figures-of-merit significantly but has little effect on

the current figure-of-merit. The reason for the increases in the pyroelectric figures-of-merit is the presence of the rapidly-decreasing relative permittivity value in the denominators

Among the major applications of piezoelectric materials are hydrophones. These are characterized by the hydrostatic or hydrophone figure-of-merit [32] and the acoustic impedance [33]. The equations for these parameters are presented in Table II and the hydrostatic figure-of-merit and the acoustic impedance are shown in Figs. 10 and 11, resp. The hydrostatic figure-of-merit is used to characterize the sensitivity of the hydrophone. Because  $d_{31}$  and  $d_{33}$  have opposite signs,  $d_h$  is relatively small for the dense material. However,  $d_{31}$  rapidly decreases with porosity and  $d_{33}$  remains constant, thus causing  $d_h$  to increase with porosity. As mentioned previously, it is desirable for the acoustic impedance of a hydrophone to match as closely as possible to that of its environment, usually air or water. Thus the acoustic impedance of the hydrophone should be as small as possible. As shown in Fig. 11, the acoustic impedance decreases strongly with increasing porosity because of the decrease in both density and elastic stiffness.

## 5. Conclusions

Measurements were made of a number of physical properties of a ferroelectric ceramic, Ferroperm® Pz27 with porosities of 20, 25 and 30%. Scanning electron micrographs showed that the materials had a mixture of 3-0 and 3-3 connectivities. The physical properties that were measured included thermal diffusivity and conductivity, heat capacity, pyroelectric coefficient, relative permittivity and loss factor, and several piezoelectric and elastic constants. Although the pyroelectric and piezoelectric coefficients diminished with increasing porosity, the pyroelectric voltage, imaging and detectivity figures-of-merit and the hydrostatic figure-of-merit increased significantly with increasing porosity and the acoustic impedance diminished. The figures-of-merit are very important for applications, suggesting that the introduction of porosity in ferroelectric ceramics opens new technological possibilities.

## 6. Acknowledgements

The authors thank J.C. Lashley (Los Alamos Scientific Laboratory) and Y.W. Wong (Hong Kong Polytechnic University) for making the heat capacity measurements.

## Figure Captions

Note: The dotted lines serve as a guide to the points and are not intended to be used for interpolation.

1. SEM photos of poled Pz27 samples: (a) dense material with 4% porosity; (b) 20% porosity; (c) 25% porosity; (d) 30% porosity. Note presence of poling fluid in (d).
2. Thermal conductivities of poled porous Pz27 samples compared to that of dense Pz27.
3. Pyroelectric coefficients of dense and porous Pz27.
4. Dielectric constants of dense and porous Pz27, as functions of frequency.
5. Dielectric loss tangents of dense and porous Pz27, as functions of frequency.
6. Piezoelectric charge coefficients of dense and porous Pz27. (a) Real components of  $d_{31}$  and  $d_{33}$ . (b)  $\tan \delta$  of  $d_{31}$ .
7. Coupling coefficients and planar Poisson's ratio of dense and porous Pz27. (a) Coupling coefficients  $k_{31}$ ,  $k_p$  and  $k_t$  and Poisson's ratio. (b)  $\tan \delta$  of the coupling coefficients.
8. Elastic stiffnesses and compliances of dense and porous Pz27. (a) Real components of elastic constants. (b)  $\tan \delta$  of elastic constants.
9. Pyroelectric voltage and current figures-of-merit.
10. Pyroelectric detectivity and imaging figures-of-merit.
11. Piezoelectric hydrostatic figures-of-merit.
12. Acoustic impedances.

TABLE I  
PYROELECTRIC FIGURES-OF-MERIT

Figure-Of-Merit	Equation
Voltage ( $\text{m}^2 \text{C}^{-1}$ )	$p / (c \rho \epsilon_0 \epsilon)$
Current ( $\text{m V}^{-1}$ )	$p / c \rho$
Detectivity ( $\text{Pa}^{-1/2}$ )	$p / [c \rho (\epsilon_0 \epsilon \tan \delta)^{1/2}]$
Imaging ( $\text{s C}^{-1}$ )	$p / (c \rho \epsilon_0 \epsilon \alpha)$

TABLE II  
PIEZOELECTRIC FIGURES-OF-MERIT

Parameter	Equation
$d_h$ ( $\text{C N}^{-1}$ )	$d_h = d_{33} + 2 d_{31}$
$g_h$ ( $\text{mV m}^{-1} \text{N}^{-1}$ )	$g_h = g_{33} + 2 g_{31}$
$d_h g_h$ ( $\text{m}^2 \text{N}^{-1}$ )	$d_h g_h$
Acoustic impedance ( $\text{kg m}^{-2} \text{s}^{-1}$ or Rayl)	$Z = (\rho c)^{1/2}$

## References

1. R. Guo, Wang C.A., and Yang A.K.: *J. Eur. Ceram. Soc.* 31, 605 (2011)
2. R. Guo, et al.: *J. Appl. Phys.* 108, 124112 (2010)
3. Z.M. He, Ma J., and Zhang R.F.: *Ceram. Int.* 30, 1353 (2004)
4. F. Levassort, et al.: *J. Electroceram.* 19, 125 (2007)
5. D. Piazza, et al.: *J. Electroceram.* 24, 170 (2010)
6. B. Praveenkumar, Kumar H.H., and Kharat D.K.: *B. Mater. Sci.* 28, 453 (2005)
7. B. Praveenkumar, Kumar H.H., and Kharat D.K.: *J. Mater. Sci.-Mater. El.* 17, 515 (2006)
8. A.N. Rybjanets, Porous Piezoelectric Ceramics - A historical overview, 2010 IEEE International Symposium on the Applications of Ferroelectrics (ISAF2010),
9. V. Stancu, et al.: *Thin Solid Films.* 515, 6557 (2007)
10. G. Suyal and Setter N.: *J. Eur. Ceram. Soc.* 24, 247 (2004)
11. R.W. Whatmore, et al.: *Phys. Scripta.* T129, 6 (2007)
12. L. Pardo, et al.: *J. Electroceram.* 19, 413 (2007)
13. C.P. Shaw, Whatmore R., and Alcock J.R.: *J. Am. Ceram. Soc.* 90, 137 (2007)
14. A.K. Yang, et al.: *J. Am. Ceram. Soc.* 93, 1984 (2010)
15. A.N. Rybjanets: *IEEE Trans. Ultrason., Ferroelect., Freq. Contr.* 58, 1492 (2011)
16. W. Wersing, Lubitz K., and Mohaupt J.: *Ferroelectrics.* 68, 77 (1986)
17. G. Suyal, Seifert A., and Setter N.: *Applied Physics Letters.* 81, 1059 (2002)
18. Meggitt Sensing Systems, <http://www.meggitt.com>
19. R.E. Newnham, Skinner D.P., and Cross L.E.: *Mat. Res. Bull.* 13, 525 (1978)
20. S.B. Lang, et al.: *IEEE T. Ultrason. Ferr.* 54, 2608 (2007)
21. S.B. Lang: *Ferroelectrics.* 93, 87 (1989)
22. S. Muensit and Lang S.B.: *Ferroelectrics.* 293, 341 (2003)
23. J.C. Lashley, et al.: *Cryogenics.* 43, 369 (2003)
24. Meggitt Sensing Systems, Ferroperm® website, <http://www.ferroperm-piezo.com>
25. S.B. Lang and Steckel F.: *Rev. Sci. Instrum.* 36, 929 (1965)
26. R.L. Byer and Roundy C.B.: *Ferroelectrics.* 3, 333 (1972)
27. A.G. Chynoweth: *J. Appl. Phys.* 27, 78 (1956)
28. M. Alguero, et al.: *J. Am. Ceram. Soc.* 87, 209 (2004)
29. R. Holland: *IEEE Trans. Sonics Ultrasonics.* SU-14, 18 (1967)
30. "IEEE Standard on Piezoelectricity", IEEE Std 176-1987, 1987
31. R.W. Whatmore: *Rep. Prog. Phys.* 49, 1335 (1986)
32. G.W. Taylor, et al.: *Piezoelectricity.* (Gordon and Breach Science Publishers London, 1985)
33. K. Uchino: *Ferroelectric Devices.* (Marcel Dekker New York, 2000)

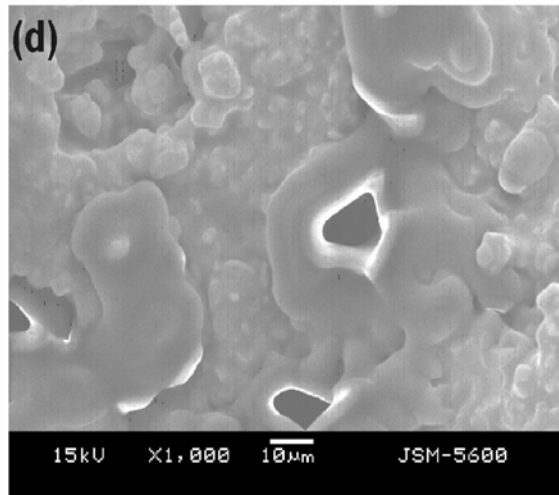
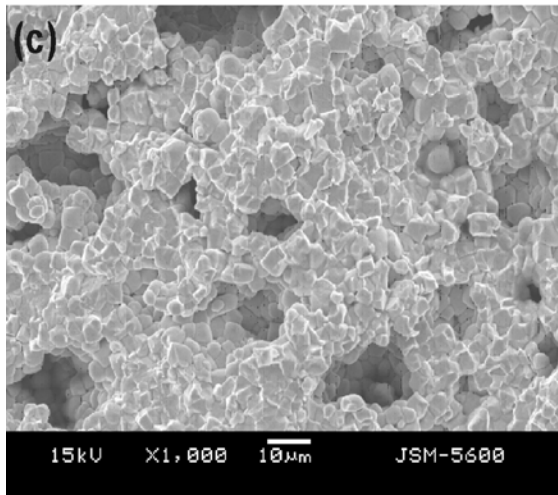
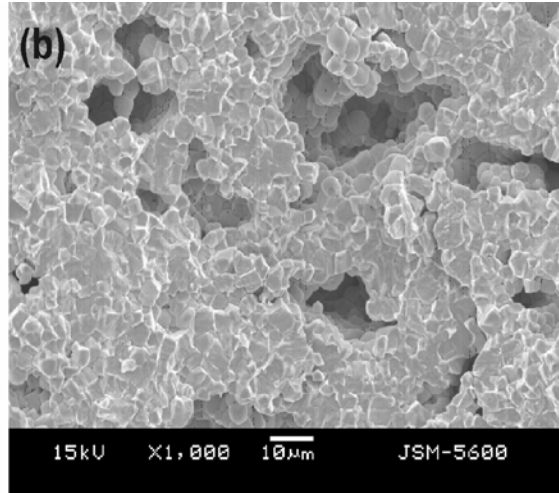
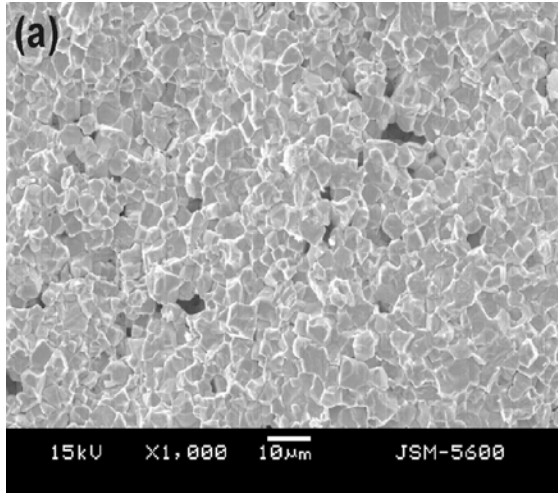


Figure 1

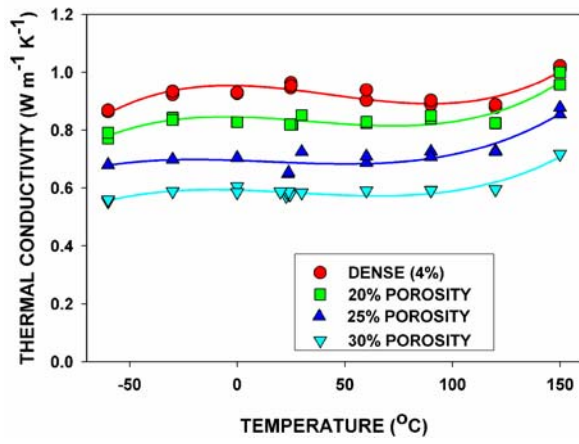


Figure 2

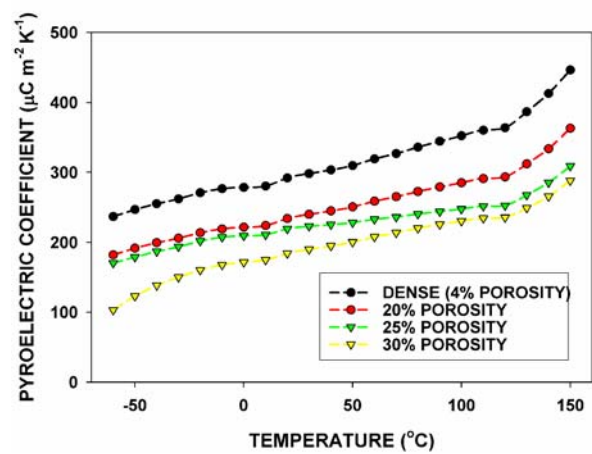


Figure 3

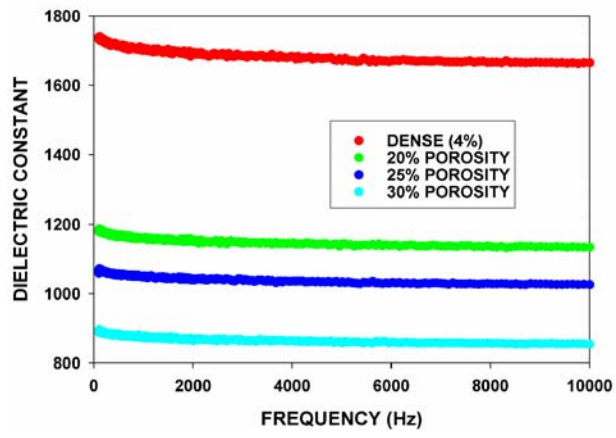


Figure 4

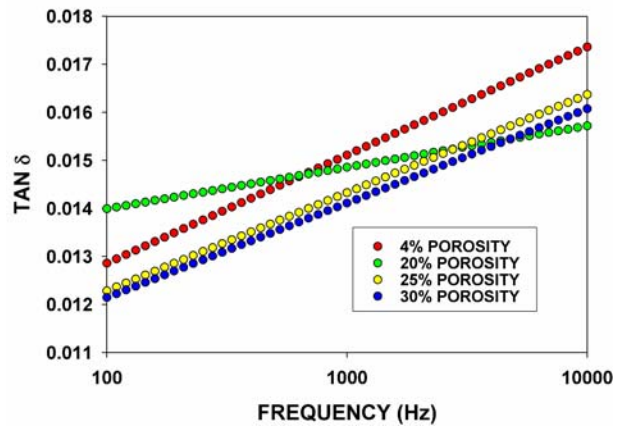


Figure 5

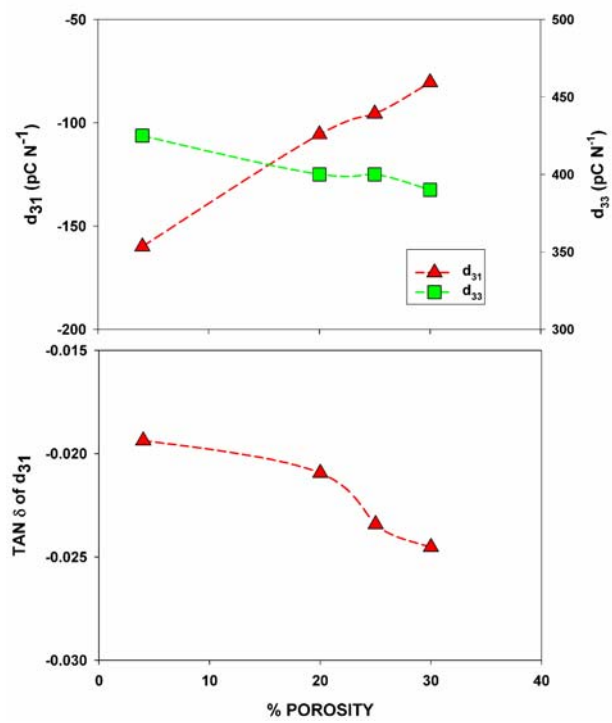


Figure 6

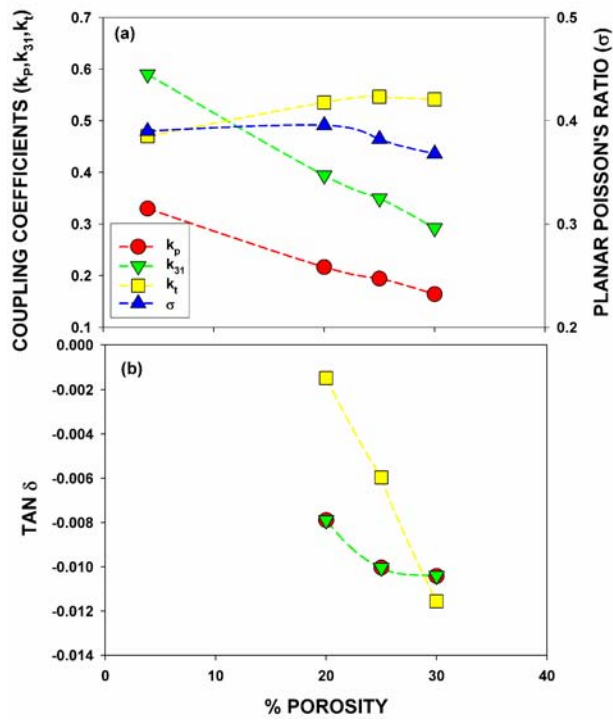


Figure 7

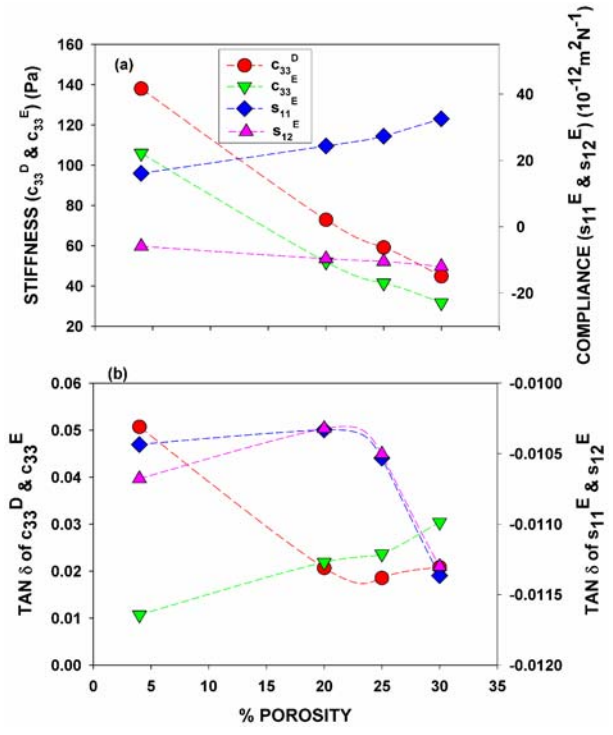


Figure 8

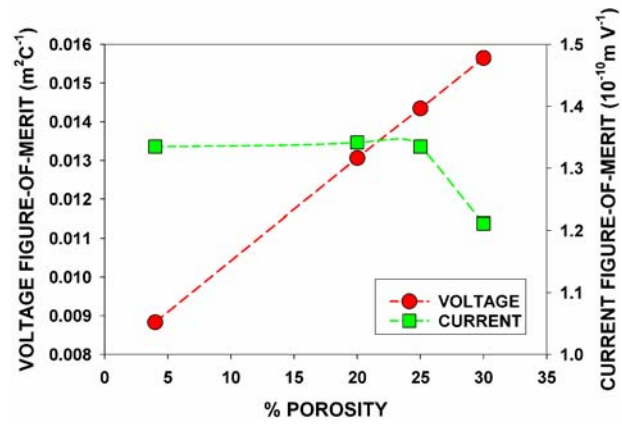


Figure 9

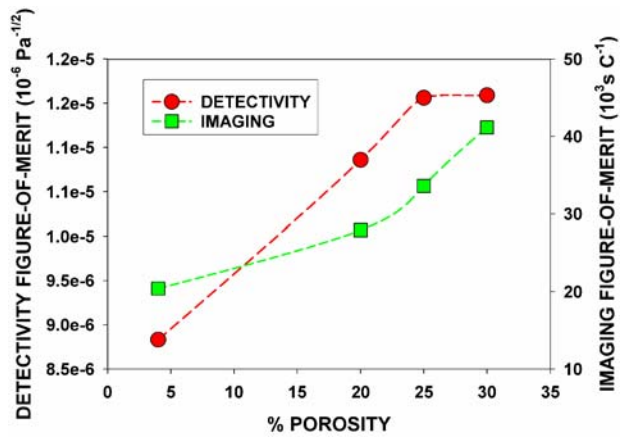


Figure 10

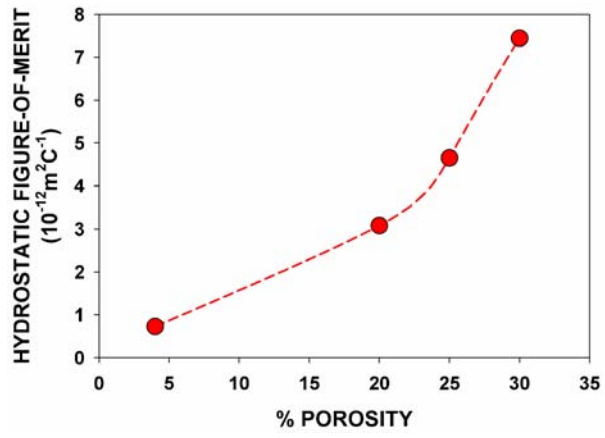


Figure 11

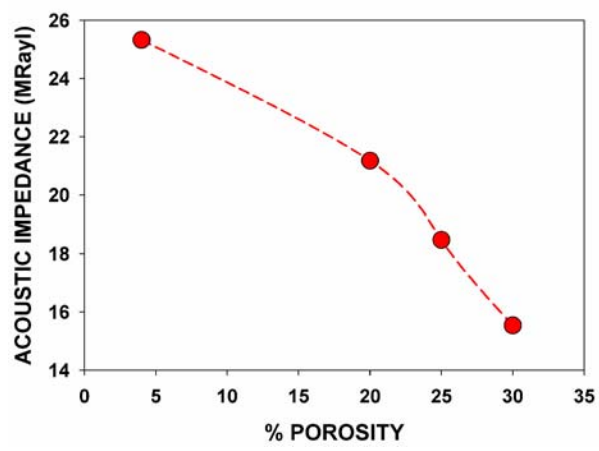


Figure 12